Model-Based Quantitative Analysis of Power Losses Aware Active Cell Balancing Networks with Load

Syed Bilal Javed[1], Ali Arshad Uppal[2], Muhammad Rizwan Azam[2] and Qadeer Ahmed[3]

***Abstract*—Cell balancing has a paramount significance in a battery management system (BMS) for improving battery performance and safety. Performance characterization of different active cell balancing networks (ACBNs) is important to understand their utilization. In this work, switching capacitor (SC), buck-boost (BB), and flyback (FB) ACBNs with static and dynamic parameters are quantitatively analyzed during charging/discharging and static conditions. For this purpose, a high-fidelity mean current modeling approach is employed, and an urban dynamometer driving schedule (UDDS) input current profile is used. The analysis of each ACBN is verified by incorporating a practical scenario in Simscape™toolbox of SIMULINK. A state dependent Kalman Filter (SDKF) is also designed to estimate the state of charge (SoC), as precise estimation of the SoC is critical for determining the performance of any balancing architecture. The sensitivity analysis manifests that consideration of static and dynamic parameters results in a percentage change of 26.75%, 80%, and 108% in the cell balancing speed of SC, BB, and FB, respectively. Furthermore, it is observed that the trade-off exhibited in the efficiency and cell balancing speed of balancing architectures. It is worth observing that the SC network is efficient but slower than BB and FB cell balancing techniques. While the BB is slower than FB but almost similar in terms of efficiency.**

***Index Terms*—Active cell balancing, Battery Pack, SoC estimator**

I. Introduction

LITHIUM cells are connected in series and parallel to meet the required voltage and power demand. The manufacturing variations and environmental conditions cause imbalance in cell's capacity and state of charge (SoC) [1], [2]. The over-voltage exposure due to cell imbalances can cause cell degradation. Moreover, the overcharged cells lead towards overheating that can cause explosion and fire in the battery pack. Various cell balancing architectures including passive and active circuits are reported in the literature [3]–[5]. Active balancing circuits are more efficient and provide fast energy transfer between cells. Herein, the energy is actively transferred between cells to get an equilibrium energy level during both the charging and discharging processes. The active balancing circuits available in the literature differ in terms of energy storage elements (i.e., inductors, capacitors, and transformers) and their interconnecting architectures [4], [6].

A. Motivation and Related Work

The primary objective of the proposed research work is to formulate control-oriented and power losses-aware active cell balancing networks. To employ model-based control, model selection plays an important role. Too complex a model can complicate the task of control design. The trade-off between the model prediction capabilities and the ease in control design is mitigated by opting mean current modeling approach, which retains the fundamental dynamics of the cell balancing process. In our previous works [7], [8], mean current modeling approaches have been employed to investigate the impact of static and dynamic parameters for a capacitor and inductor based cell balancing techniques, respectively. The static parameters mainly include resistances of cells, switch and energy storage elements, and diode forward voltage drop. The dynamic parameters comprise the dead time, rise time, and fall time.

In most of the literature, qualitative analysis is carried out to evaluate the performance of the active cell balancing networks (ACBNs) in terms of balancing time, circuit complexity, and efficiency. In [5], different active balancing methods are grouped according to their circuit topology, and their merits and demerits in terms of balancing cost, complexity, preferred application, and modular design, are compared. The authors in [9] have presented a detailed review on various cell balancing techniques for Li-ion batteries. The cell equalization techniques are qualitatively analyzed and compared against cost, balancing speed, complexity of the architecture, and application. In [10], various topologies of ACBNs are compared, and the multiple inductor-based approach is discussed in detail. A number of factors, such as circuit design, voltage/current stress, balancing speed, architecture complexity, size, cost, and balancing efficiency, are considered for comparison.

The authors in [11], developed mathematical models of various active equalization structures to describe their dynamic behavior. The performance of nine active equalization circuits is qualitatively evaluated through extensive numerical simulations, with a comprehensive comparison made amongst them based on factors such as balancing speed, cost, control complexity, efficiency, and weight/size. The authors in [12] provide a comparative analysis of various DC-DC converter-based topologies and control strategies used for battery charge equalization. The authors provide extensive simulation results comparing the performance of different topologies in

*This work was not supported by any organization

S. B. Javed[1] is with Centers of Excellence in Science & Applied Technologies, Islamabad, Pakistan, s.bilal.javed@gmail.com

A. A. Uppal[2] and M. R. Azam[2] are with the Department of Electrical and Computer Engineering, COMSATS University Islamabad, Islamabad 44000, Pakistan. ali_arshad@comsats.edu.pk, rizwan.azam@comsats.edu.pk.

[3]Qadeer Ahmed is with the Department of Center for Automotive Research, The Ohio State University, Columbus, OH 43210 USA ahmed.358@osu.edu

balancing speed, balancing time, size, cost, power loss, and efficiency. Moreover, similar studies are conducted in [4], [13]–[16], where a qualitative comparison is performed for different active balancing circuits on the basis of balancing cost, efficiency, speed, preferred application, and complexity of the balancing architecture.

Depending on the application, the selection of an optimal balancing architecture and the most suitable electronic component parameters poses a great challenge. The qualitative analysis conducted in the above literature is not sufficient to highlight the effectiveness of different proposed solutions. In this regard, some of the recent literature also covers the quantitative analysis of active cell balancing techniques c.f., [17]–[20]. The authors in [17] compared the balancing time and associated energy losses of seven different balancing architectures. A generalized analytical model is used in [18] to calculate the performance of various balancing architectures on the basis of balancing time and energy losses as a function of efficiency and the initial charge imbalance. The authors in [19] applied a mean current model-based approach to perform a comprehensive quantitative analysis for 10 active balancing circuits. They extended their research in [20] to include the dynamic charge/discharge operations in the context of an electric vehicle, and the effect of various control algorithms on battery efficiency. The article in [21] provides a detailed comparison between a passive balancing system with an inductor based active balancing system on the basis of simulations. The focus of the comparison is the battery efficiency and balancing speed for various vehicular applications. The battery efficiency is measured in terms of the power, energy losses and temperature changes.

B. Gap Analysis

Based on the literature review, the following research gaps have been identified:

1) Quantitative analysis of ACBN has been presented for the ideal cell balancing networks, simplifying the model formulation of ACBN by ignoring the static and dynamic parameters. To perform in-depth quantitative analysis, high fidelity models of cell balancing architectures are essential.
2) In practice, the analysis based on ideal networks can not be a true depiction of the real cell balancing network because it does not account for power losses. The efficiency and cell balancing speed of any cell balancing network are sensitive to the real circuit parameters and load conditions. Furthermore, only the static condition for cell balancing is considered to draw the comparison and ignore the load i.e. charging/discharging conditions. Thus, to accurately characterize ACBN, it is important to incorporate both static and dynamic parameters under static and load conditions.
3) Along with the missing quantitative analysis with static and dynamic parameters, various topologies of capacitive, inductive, and transformer-based ACBNs are compared individually in the literature. However, a generalized analysis to compare the performance of all the topologies of each ACBNs is currently lacking due to the reasons highlighted earlier.
4) The ACBN models discussed in the literature do not incorporate control design or focus on control-oriented modeling. The control design is essential to minimize the balancing speed and power losses of ACBN. This will help to improve accuracy, efficiency, performance, economic benefits, and safety of a battery pack.

C. Major Contributions

The major contributions of the proposed work are outlined below.

1) Formulation of high-fidelity mean current models considering static and dynamic parameters for switching capacitor (SC), buck-boost (BB), and flyback (FB) networks are presented in section III. Furthermore in section IV, each ACBN is validated by implementing them at the schematic level, incorporating practical considerations, in the Simscape™toolbox of SIMULINK.
2) The proposed models are capable of evaluating static and dynamic power losses in ACBN, making them useful for ACBN characterization. In section V, the performance of each ACBN is determined in a practical scenario, considering measurement and process noises under both static and dynamic load conditions.
3) The analysis of each ACBN is generalized and applicable to n-series connected cells battery pack, as demonstrated in section V by the implementation of the proposed models for a three-series connected Li-ion cells.
4) The proposed models are computationally efficient and suitable for designing closed-loop system for thermal management and to minimize the power losses and balancing speed of ACBN, as described in our previous work [8], [22].

The manuscript is organized in the following manner. The equivalent circuit model (ECM) of the cell is discussed in section II. In section III, the high fidelity mean current modeling of the ACBNs is presented. The simulation results are demonstrated and discussed in section V, whereas, the article is concluded in section VI.

II. Equivalent Circuit Model of the Battery Cell

In this article, a second-order Thevenin model is adapted to represent the ECM of the cell. The schematic of the cell is shown in Fig. 2a, and its state space model is given as

$$\dot{x} = A(x)x + B(x)i + w(t), \tag{1}$$

$$A(x) = \begin{bmatrix} -\dfrac{1}{R_1(x_3)C_1(x_3)} & 0 & 0 \\ 0 & -\dfrac{1}{R_2(x_3)C_2(x_3)} & 0 \\ 0 & 0 & 0 \end{bmatrix},$$

$$B(x) = \begin{bmatrix} \dfrac{1}{C_1(x_3)} & \dfrac{1}{C_2(x_3)} & -\dfrac{1}{\eta} \end{bmatrix}^T,$$

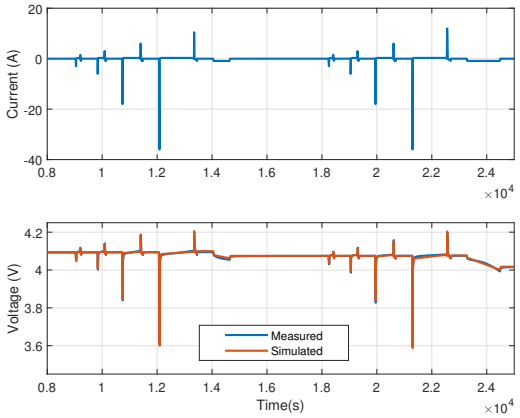

Fig. 1: Pulse charge and discharge characterization data, and measured and simulated voltages

where $x^T = \begin{bmatrix} V_{c1} & V_{c2} & SoC \end{bmatrix}$ represents the state vector; $R_1(x_3)$ and $C_1(x_3)$ are electro-chemical polarization resistance and capacitance, respectively; $R_2(x_3)$ and $C_2(x_3)$ are concentration polarization resistance and capacitance, respectively [23]; i, $w(t)$ and η represent charging/discharging current, the process noise, and nominal cell capacity, respectively.

From Fig. 2a the terminal voltage of the cell (V_T) is characterized as

$$V_T = V_{OC}(x_3) - R_0(x_3)i - x_1 - x_2 + \phi(t), \tag{2}$$

where V_{OC} is the open circuit voltage; R_0 is the internal resistance of the cell; and $\phi(t)$ is the measurement noise.

The mathematical model of the cell represented by (1) and (2) is nonlinear due to the dependency of the parameters on x_3. The remaining section is dedicated to the estimation of the x_3 dependent model parameters. The parameters used in this model, i.e., V_{OC}, resistances, and capacitances must be identified from the actual battery cell data. The model has been fitted using experimental data collected from a 3Ah, 3.6 V LG 18650 HG2 NMC cell [24]. The parameter vector θ contains five independent parameters to be identified i.e.,

$$\theta = [R_0(x_3)\ R_1(x_3)\ C_1(x_3)\ R_2(x_3)\ C_2(x_3)]^T, \tag{3}$$

where the parameters are dependent on x_3. The model is constructed using the Simscape™environment that allowed us to connect our model with the SIMULINK design optimization toolbox. A least-squares estimation algorithm is employed to identify the optimal parameter vector θ. A specialized high power pulse charging (HPPC) test has been performed at room temperature to characterize the cell dynamics (voltage response) at various C rates. The test comprises 1, 2, 4, and 6C discharge current pulses and 0.5, 1, 1.5, and 2C charge current pulses, each followed by a relaxation period as illustrated in Fig. 1. This set of pulses is continuously applied until the cell is fully discharged i.e., covers the complete SoC range. For model validation the urban dynamometer driving schedule (UDDS) and the California unified cycle (LA-92) drive cycles are used, which yield mean absolute error between measured and simulated voltages of 3.6% and 4.4%, respectively.

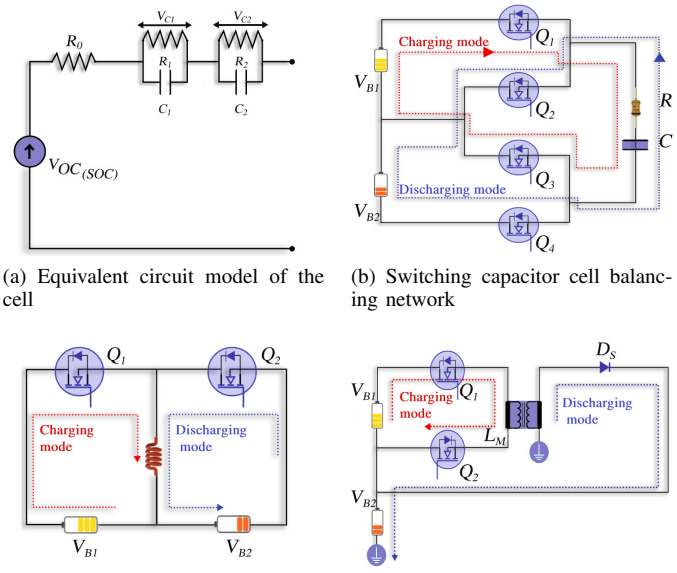

(a) Equivalent circuit model of the cell

(b) Switching capacitor cell balancing network

(c) Buck-boost cell balancing network

(d) Flyback cell balancing network

Fig. 2: Schematic diagram of the equivalent circuit model of ACBNs for cell-to-cell balancing

III. Modeling of Active Cell Balancing Architectures

In this paper, a simple architecture comprising one energy storage element and two series-connected cells is considered to formulate the model equations for each cell-to-cell ACBN. These model equations can be generalized for an n-series-connected cell battery pack, as the transfer of charge among two cells always require one energy storage element. In cell-to-cell charge transfer, the static and dynamic parameters in the charging and discharging paths of each ACBNs are similar; therefore, this analysis can be extended to other capacitor, inductor, and transformer-based cell balancing architectures.In this work, the contribution comes by considering the mean balancing current approach to formulate the model of each ACBNs. Generally, the transfer of charge between cells occurs at high rates per second (f) with repeated cycles, and the net transfer of charge by balancing currents in one switching cycle is negligibly smaller as compared to the charge stored in battery cells. The model formulation of each ACBN is discussed in the following sections and a list of symbols is presented in Table I.

A. Switching capacitor network

There are numerous capacitor based cell balancing techniques such as switched capacitor (SC), double-tiered capacitor, and flying capacitor configurations. In the SC architecture, $2N$ switches and $N-1$ capacitors are required to balance a battery pack with N series-connected cells. A simple SC architecture comprising one capacitor and two series-connected cells is considered to formulate the model equations, as shown in Fig. 2b. The switches ($Q_1 = Q_3 = Q$, $Q_2 = Q_4 = \bar{Q}$) are controlled by a simple pulse-width modulation (PWM) signal having duty cycle (D) and switching period (T). While V_{B_1} and V_{B_2} represent the cells having higher and lower voltages,

TABLE I: List of symbols for cell balancing netwroks

Symbol	Description
Q_i	Switches
f	Switching frequency (Hz)
T	Switching time period (sec)
t_o	Time instant at which the inductor current reaches to zero level (sec)
D, SoC	Duty cycle and state of charge, respectively (%)
t_d, t_r, t_f	Dead time, rise time and fall time, respectively (sec)
V_{B_1}, V_{B_2}	Cell with higher and lower voltages, respectively (V),
R_{ds}, R_{ch}, R_{dis}	On-state switching resistance and net resistance of charging and discharging paths of energy storage elements, respectively (Ω)
$\tilde{I}$, I	Mean current and effective currents, respectively (A)
$\tilde{I}_{out}$, $\tilde{I}_{in}$	Mean current during charging and discharging of inductive elements (A)
I_{ch}, I_{dis}	Effective current during charging and discharging modes of SC, buck-boost and fly-back converters, respectively (A)
I_{RR}, I_P	Reverse recovery current of body diode and maximum current of inductive balancing architectures, respectively (A)
$\bar{P}_{con}$, P_{t_r}, P_{t_f}	Power conduction losses and switching power losses during the turn-on and turn-off process of MOSFET, respectively (W)
$P_{D_{RR}}$, P_{t_d}	Reverse recovery loss in the body diode and power loss due to dead time, respectively (W)
V_T, V_{OC}	Terminal voltage and open circuit voltage of cell, respectively (V)

respectively. In our previous work [7], the working of SC architecture has been discussed in detail. The control algorithm and capacitor's voltage and current profiles are shown in Fig. 3. Under steady-state conditions, the voltage across the capacitor during each mode is given as

$$v_c(t) = \begin{cases} V_1, & 0 \le t \le t_d, \\ V_{B_1} + (V_1 - V_{B_1})e^{-(t-t_d)/\tau}, & t_d \le t \le DT, \\ V_2, & DT \le t \le DT + t_d, \\ V_{B_2} - (V_{B_2} - V_2)e^{-(t-DT-t_d)/\tau}, & (DT + t_d) \le t \le T, \end{cases} \tag{4}$$

where V_1 and V_2 are computed by solving the set of above equations and are given as

$$V_1 = \frac{1}{1-e^{\alpha}}\left[V_{B_1}\left(e^{\beta} - e^{\alpha}\right) + V_{B_2}\left(1 - e^{\beta}\right)\right], \tag{5}$$

$$V_2 = \frac{1}{1-e^{\alpha}}\left[V_{B_1}\left(1 - e^{\gamma}\right) + V_{B_2}\left(e^{\gamma} - e^{\alpha}\right)\right], \tag{6}$$

where $\alpha = \dfrac{2t_d - T}{\tau}$, $\beta = \dfrac{t_d - T(1-D)}{\tau}$, $\gamma = \dfrac{t_d - DT}{\tau}$, and $\tau = RC$ represent the voltage transients and time constant, respectively. During charging and discharging modes, two switches are included in each mode, therefore, R is characterized as

$$R = R_c + 2R_{ds} + R_o, \tag{7}$$

where R_c and R_o are the capacitor's parasitic resistance and internal resistance of the cell, respectively.

1) Mean balancing Current

The mean value of capacitor current can be expressed as

$$\tilde{I} = \frac{\Delta Q}{T} = \frac{C}{T}\Delta V, \tag{8}$$

where ΔV is the voltage ripple and C is the capacitor size. It is evident in (8) that $\tilde{I}$ is the highest at the maximum ripple voltage condition for the SC network. The analysis of (4)

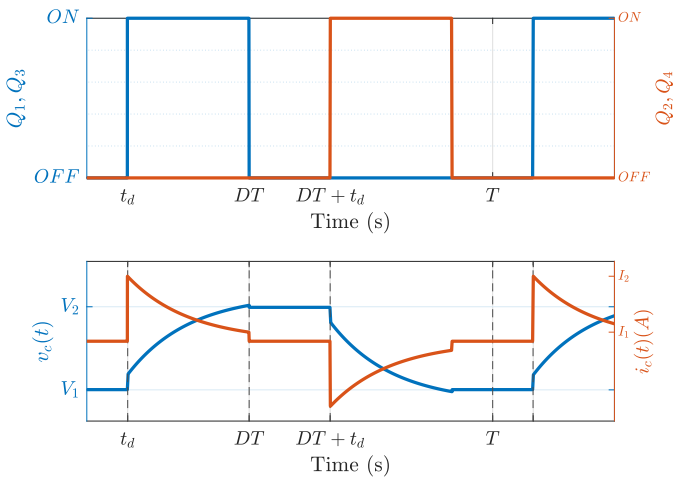

Fig. 3: Control algorithm, voltage and current profiles of SC network

shows that the maximum ripple voltage occurs at $D = 0.5$ and it can be expressed as

$$\Delta V = (V_{B_1} - V_{B_2})\, Tanh\left(\frac{0.5T - t_d}{2\tau}\right). \tag{9}$$

Hence, the mean current for a single time interval of the length $T/2$ becomes

$$\tilde{I} = \frac{C}{T}(V_{B_1} - V_{B_2})\, Tanh\left(\frac{0.5T - t_d}{2\tau}\right). \tag{10}$$

This is the fundamental expression of $\tilde{I}$ which shows that the performance of the SC network is a function of all parasitic, static, and dynamic parameters. Moreover, it also includes switching frequency and cell imbalance voltages.

2) Power losses

In the SC network, conduction and switching losses account for the total power losses. The conduction power losses are caused by the on-state resistance of MOSFETs, diodes, the parasitic resistance of energy storage elements, and cell internal resistance. The conduction losses during the entire operation of the balancing network are

$$\bar{P}_{con} = 2I^2RD \tag{11}$$

where, I is the effective value of current, R is the net resistance of the conduction path and D is the duty cycle. The expressions of I for charging and discharging modes of the capacitor are derived by using (4), and are given in (12) and (13), respectively.

$$I_{ch} = \sqrt{\frac{\tau(V_{B_1} - V_1)^2}{2TR^2}\left[1 - e^{\frac{-2(DT - t_d)}{\tau}}\right]}, \tag{12}$$

$$I_{dis} = \sqrt{\tau\frac{(V_{B_2} - V_2)^2}{2TR^2}\left[e^{\frac{2(t_d + DT - T)}{\tau}} - 1\right]}, \tag{13}$$

where I_{ch} and I_{dis} are the effective currents during the charging and discharging modes of the capacitor, respectively. The power losses that occur due to switching in each MOSFET

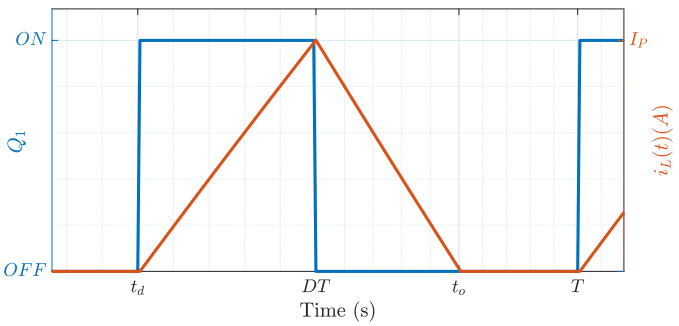

Fig. 4: Control algorithm and inductor current profile of buck-boost cell-balancing technique

of the SC network are computed by using the piece-wise linear functions. The expressions of switching losses of each MOSFET due to the rise time and fall time are derived in our previous work [7].

B. Buck-boost configuration

The switching inductor and BB configurations are the most common inductive-based cell balancing techniques. The BB configuration for two series connected cells is shown in Fig. 2c. This configuration has two operating modes, defined by the charging and discharging of the inductor. The switch Q_1 is closed and switch Q_2 is open during the charging mode, and energy is transferred from the higher voltage cell to the inductor. While in discharging mode of the inductor, both switches remain in the off state and the inductor discharges through the free-wheeling diode. The converter is operated in a discontinuous current mode (DCM) to ensure the complete transfer of energy. The switching and inductor current profiles are shown in Fig. 4. The inductor current during the charging and discharging modes is given as

$$i(t) = \begin{cases} \frac{V_{B_1}}{R_{ch}}(1-e^{\lambda}), & t_d \le t \le DT \\ I_P e^{\varphi} + \frac{V_{B_2}+V_D}{R_{dis}}(e^{\varphi}-1), & DT \le t \le t_0 \\ 0, & elsewhere, \end{cases} \tag{14}$$

where $\lambda = \frac{-(t-t_d)}{\tau_{ch}}$, $\varphi = \frac{-(t-DT)}{\tau_{dis}}$; τ_{ch} and τ_{dis} are the time constants of charging and discharging paths, respectively; while $R_{ch} = R_0 + R_L + R_{ds}$ and $R_{dis} = R_0 + R_L$ represent the resistances of charging and discharging paths, and R_L is the parasitic resistance of inductor. The maximum current occurs at $t = DT$ and it is given as

$$I_P = \frac{V_{B_1}}{R_{ch}}(1-e^{\kappa}), \quad \kappa = \frac{-(DT-t_d)}{\tau_{ch}} \tag{15}$$

1) Mean balancing Current

The average currents during both the charging and discharging modes of the inductor are determined by integrating (14) as

$$\tilde{I}_{out} = \frac{V_{B_1}}{TR_{ch}}\left(DT - t_d + \tau_{ch}(e^{\kappa}-1)\right), \tag{16}$$

$$\tilde{I}_{in} = \frac{\tau_{dis}\,(e^{\chi}-1)}{T}\left[-I_P - \frac{a_0(t_0-DT)}{\tau_{dis}\,(e^{\chi}-1)} + 1\right], \tag{17}$$

where $\chi = \frac{-(t_0-DT)}{\tau_{dis}}$, $a_0 = \frac{V_{B_2}+V_F}{R_{dis}}$ and D is the minimum condition for the duty cycle to ensure DCM operation.

The time instant at which the inductor current becomes zero is represented by $t = t_0$, and the expression is determined by solving (14) for the discharging mode of the inductor.

$$t_0 = DT + \tau_{dis} ln\left[\frac{R_{dis}V_{B_1}}{(V_{B_2}+V_F)R_{ch}}(1-e^{\kappa})+1\right].$$

It is evident in (16) and (17) that the performance of the buck-boost converter depends on switching frequency and cell imbalance voltages, and it is also a function of all parasitic, static, and dynamic parameters.

2) Power losses

The following factors contribute to power losses in an inductive-based cell-balancing network:

- Conduction losses are caused by the on-state resistance of MOSFETs, diodes, the parasitic resistance of energy storage elements, and cell internal resistance.
- Switching losses in the MOSFETs due to rise time and fall time.
- Reverse recovery losses in the body diode.
- Power losses due to the dead time.

a) Conduction and switching losses

The conduction losses during the entire operation of the balancing network are

$$\bar{P}_{con} = I_{ch}^2 R_{ch} D + I_{dis}^2 R_{dis}\frac{t_0 - DT}{T}, \tag{18}$$

where I_{ch} and I_{dis} represent the effective currents during the charging and discharging modes of inductor, respectively. The expressions of I_{ch} and I_{dis} are

$$I_{ch}^2 = \frac{{V_{B_1}}^2}{T{R_{ch}}^2}\left[\tau_{ch}e^{\kappa}\left(\frac{4-e^{\kappa}}{2}\right) + DT - t_d - \frac{3\tau_{ch}}{2}\right], \tag{19}$$

$$I_{dis}^2 = \frac{e^{\chi}\tau_{dis}}{T}\left[2a_0\left(I_P + a_0\right) - e^{\chi}\left(\frac{I_P^2}{2} + \frac{a_0^2}{2} + a_0 I_P\right)\right] + \frac{\tau_{dis}I_P}{T}\left(\frac{I_P}{2} - a_0\right) + \frac{a_0^2}{T}\left(t_0 - DT - \frac{3}{2}\tau_{dis}\right). \tag{20}$$

As an inductive cell balancing network is operated in DCM, switching power losses during turn-on time are negligible and can be neglected. The switching power losses during the turn-off process are computed by assuming the linear behavior of voltage and current and can be characterized as

$$P_{t_f} = \frac{1}{2T}V_{B_1}\tilde{I}_{in}t_{fall}, \tag{21}$$

where t_{fall} is the fall time of switching and P_{t_f} is the switching power losses during the turn-off process of MOSFET.

b) Reverse recovery loss in the body diode

When the MOSFET Q_1 is turned ON, the transition of the body diode of the low-side MOSFET Q_2 from the forward biased to the reverse direction causes a diode recovery, resulting in a reverse recovery loss in the body diode. This loss is determined by the reverse recovery time of the diode (t_{RR}), and given as

$$P_{D_{RR}} = \frac{1}{2T}V_{B_2}I_{RR}t_{RR}, \tag{22}$$

where

$$I_{RR} = \sqrt{2Q_{RR}\frac{di(t)}{d(t)}}, \quad Q_{RR} = 0.5\frac{di(t)}{dt}{t_{RR}}^2,$$

where Q_{RR} is the reverse recovery charge and $\frac{di(t)}{dt} = \frac{V_{B_2}+V_F}{L}$ is the slope of straight line approximation.

c) Dead time loss

When both the MOSFETs are turned on simultaneously, a short circuit occurs and produces a very large spike of current. The dead time is used to prevent such current spikes. During t_d, the inductor current continues to flow through the body diode of the low-side MOSFET. The dead time loss is calculated as

$$P_{t_d} = \frac{1}{2T}V_F\tilde{I}_{in}t_d. \tag{23}$$

C. Flyback Converter

A flyback converter with a single-winding transformer-based balancing architecture is shown in Fig. 2d. Each transformer winding is connected in series with a switch to realize the bidirectional energy flow. The switched transformer balancing network has two operating modes. The first mode begins at $t = 0$, switches Q_1 and Q_2 are closed and energy is extracted from the highest voltage cell (V_{B_1}) and stored in the magnetizing inductance (L_M) of the transformer. During the second mode of operation at $t = DT$, all switches are turned off and the polarity of inductor voltage is reversed. Subsequently, diode D_s becomes forward biased, and current begins to flow through the secondary winding of the transformer, resulting in a transfer of energy from L_M to the lowest voltage cell (V_{B_2}). The current during each mode is expressed as

$$i(t) = \begin{cases} \frac{V_{B_1}}{R_{ch}}(1-e^{\lambda}), & t_d \le t \le DT \\ \frac{I_P}{n}e^{\varphi/n} + \frac{V_{B_2}+V_{F_S}}{nR_{dis}}\left[e^{\varphi/n}-1\right], & DT \le t \le t_0 \\ 0, & elsewhere, \end{cases} \tag{24}$$

where $R_{ch} = R_0 + 2R_{ds} + R_P$ and $R_{dis} = R_0 + R_S$ are the net resistances during the charging and discharging modes, respectively. R_0, R_{ds}, R_P, and R_S represent the resistances of the cell, switch and primary and secondary winding resistances of the transformer, respectively. While V_{F_S} is the forward voltage drop of diode D_S and $n = \frac{V_{B_2}+V_{F_S}}{V_{B_1}}$ is the turns ratio of the transformer. The maximum current occurs at $t = DT$, and it is given as

$$I_P = \frac{V_{B_1}}{R_{ch}}(1-e^{\kappa}) \tag{25}$$

.

1) Mean balancing current

The average currents during charging mode ($\tilde{I}_{out}$) and discharging mode ($\tilde{I}_{in}$) are computed by integrating (24), and given as

$$\tilde{I}_{out} = \frac{V_{B_1}}{TR_{ch}}\left(DT - t_d + \tau_{ch}(e^{\kappa}-1)\right), \tag{26}$$

$$\tilde{I}_{in} = \frac{\tau_{dis}\left(e^{\chi/n}-1\right)}{T}\left[-I_P - \frac{a_1(t_0-DT)}{\tau_{dis}\left(e^{\chi/n}-1\right)} + n\right], \tag{27}$$

where $a_1 = \frac{V_{B_2}+V_{F_S}}{nR_{dis}}$ and t_0 is the time instant at which the current reaches at zero level, and it is given by

TABLE II: List of Parameters

Parameters used in cell balancing architectures.			
C	47 μ F	R_c	10 $m\Omega$
L	6.0 μ H	R_L	10 $m\Omega$
L_M	6.0 μ H	R_P	10 $m\Omega$
f	50 kHz	R_S	10 $m\Omega$
D	40%	R_o	44.1 $m\Omega$
t_d	2 μs	R_{ds}	5.3 $m\Omega$
t_r	72 ns	V_F	0.3 V
t_f	8 ns	V_{F_S}	0.3 V

2) Power losses

Power losses in a transformer-based cell balancing network are calculated in the same way as derived for the buck-boost configuration. The set of equations for the effective value of current during charging and discharging mode of magnetizing inductance are given below.

$$I_{ch}^2 = \frac{{V_{B_1}}^2}{T{R_{ch}}^2}\left[\tau_{ch}e^{\kappa T}\left(\frac{4-e^{\kappa}}{2}\right) + DT - t_d - \frac{3\tau_{ch}}{2}\right], \tag{28}$$

$$I_{dis}^2 = \frac{e^{\chi/n}\tau_{dis}}{T}\left[2a_1(I_P+na_1) - e^{\chi/n}\left(\frac{I_P^2}{2n} + \frac{na_1^2}{2} + a_1I_P\right)\right] + \frac{\tau_{dis}I_P}{T}\left(\frac{I_P}{2n} - a_1\right) + \frac{a_1^2}{T}\left(t_0 - DT - \frac{3}{2}n\tau_{dis}\right). \tag{29}$$

The conduction and switching power losses are

$$\bar{P}_{con} = I_{ch}^2R_{ch}D + I_{dis}^2R_{dis}\frac{t_0-DT}{T}, \tag{30}$$

$$P_{t_f} = \frac{1}{2T}V_{B_1}\tilde{I}_{in}t_{fall}, \quad P_{t_d} = \frac{1}{2T}\left(V_{B_2}+V_{F_S}\right)\tilde{I}_{in}t_d. \tag{31}$$

where $\bar{P}_{con}$, P_{t_f}, P_{t_d} are the conduction power losses, switching power losses during the turn-off process of switches and the power loss during dead time, respectively . Since no current flows through the body diode in reverse direction, therefore, the reverse recovery loss in the body diode is not computed for this balancing network.

IV. Model Validation

All active cell balancing networks are implemented in the Simscape™ toolbox of SIMULINK to validate the analytical results of each ACBN. For model validation, a practical scenario is incorporated in the Simscape™by considering two series connected cells which are imbalanced by $300mV$ and their voltages are $4.0V$ and $3.7V$, respectively. Moreover, the static and dynamic parameters are also considered in the simulation. Table II includes a list of the ACBNs' parameters. The design parameters such as capacitance, inductance, and magnetizing inductance, are selected to guarantee fair comparison by ensuring that the mean current of all the networks is comparable in a base case scenario, as explained in the section V. Furthermore, the duty cycle, switching frequency, and parasitic resistances are kept constant in all the networks. The simulation and analytical results are quantitatively compared by computing the absolute error (AE). In Table III, it is evident that analytical and simulation results perfectly match each other.

TABLE III: Verification of Mean current models of ACBNs

	Charging mode mean current $(\tilde{I}_{out}(A))$		
	Model	Simscape™	AE (%)
SC	0.5874	0.5324	5.5
Buck-boost	0.5883	0.5735	1.5
Flyback	0.5873	0.5735	1.4
	Discharging mode mean current $(\tilde{I}_{in}(A))$		
SC	0.5874	0.5324	5.5
Buck-boost	0.5883	0.5735	1.5
Flyback	0.5437	0.5438	2.99

V. Results and Discussion

In this section, simulation results are presented to show the impact of real conditions on the performance of the balancing architecture. A practical scenario is implemented in the Simscape™ toolbox of SIMULINK by incorporating the following considerations.

- The static and dynamic load i.e. charging/discharging operating conditions are considered to perform cell balancing.
- The static parameters like resistances of energy storage elements, switches, and battery cells are considered.
- The dynamic parameters in the form of dead time, rise time, and fall time are also included.
- The imbalance in battery cells is presented by considering distinct SoC for each cell.
- For SoC estimation, the SDKF of [8] is used. The process (w) and measurement (ϕ) noises are considered during simulation studies. A zero-mean, Gaussian white distribution, with a variance of 10^{-2} represents w and ϕ.
- An urban dynamometer driving schedule (UDDS) input current profile is considered to assess the performance of ACBNs during dynamic load conditions.

The implementation of the proposed schemes for N cells battery pack is shown in Fig. 5. The impact of static and dynamic parameters on the cell balancing speed and efficiency of each ACBN is discussed in following subsections.

A. Effect of Static and Dynamic Parameters on Cell Balancing Speed

A practical scenario is incorporated by performing cell balancing during charging/discharging and static operating conditions. For this purpose, three series cells ($N = 3$ in Fig. 5) with distinct SoCs are considered and UDDS current profile presented in our previous work [8] is applied to determine the performance of each ACBN. In cell-to-cell balancing $N = 3$ represents the most complex scenario, where the second cell sandwiched between first and third cell can simultaneously transfer/receive charge to/from its neighbours. The parameters of ACBNs are listed in Table II. The cell balancing speed in the worst-case scenario is determined by taking into account the first and last cells at the largest and lowest SoC levels, respectively. As shown in Fig. 5, the supervisory controller balances the SoC levels of the cells until a prescribed balancing criterion is met–SoC between first and last cells is less than or equal to 2%. An SDKF is designed for the estimation of the SoC of each battery cell, and it is illustrated in

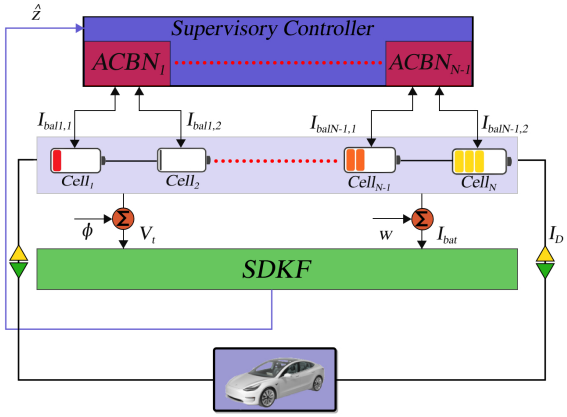

Fig. 5: Active cell balancing of N series connected cells with $N-1$ ACBNs. Here $I_{bal_{j,k}}$ is the mean charging/discharging current of a cell, and $V_t \in \Re^N$, $I_{bat} \in \Re^N$ and $\hat{z} \in \Re^N$ represent the vectors of terminal voltages, cell currents, and estimated SoC levels of each cell, respectively.

detail in our previous work [8]. The cell balancing speed of ideal and non-ideal ACBNs is compared in Fig. 6. It is evident that each ACBN's cell balancing speed is significantly impacted by both static and dynamic parameters. In Fig. 6a and Fig. 6b, it is observed that a practical SC network takes an additional 122 minutes in comparison to an ideal SC network. The comparison between ideal and non-ideal BB networks is shown in Fig. 6c and Fig. 6d, respectively, and a disparity of 64 minutes is found in the cell balancing time. Similarly, the cell balancing time of ideal and non-ideal FB networks differs by 53 minutes, as shown in Fig. 6e and Fig. 6f, respectively. The corresponding mean currents of each cell of practical ACBN are shown in Fig. 7. The cell balancing is performed during charging/discharging and static modes. To ensure fair comparison amongst all ACBNs, the initial value of mean currents is kept similar in each case by choosing the appropriate values of capacitance, inductance, and magnetizing inductance in the SC, BB, and FB netwroks, respectively.

B. Effect of Static and Dynamic Parameters on efficiency

As the proposed modeling approach is generalized and applicable for N series-connected cells battery pack. In order to simplify the analysis, a simple battery pack with two cells is considered to investigate how static and dynamic parameters affect the efficiency of a balancing network. These cells are imbalanced by $300mV$ and have voltages of $4.0V$ and $3.7V$, respectively. To compare the active cell balancing architectures, a base case is considered in which the duty cycle, switching frequency, and parasitic resistances are kept similar in each balancing network. To ensure a fair comparison, it is pertinent to mention that the average current is also kept constant in the base case by choosing the appropriate values of capacitance, inductance, and magnetizing inductance in the SC, BB, and FB converters, respectively. The percentage efficiency of an active cell balancing technique is

$$\eta = \left[1 - \frac{\bar{P}_{losses}}{\bar{P}_{in}}\right] 100\%, \tag{32}$$

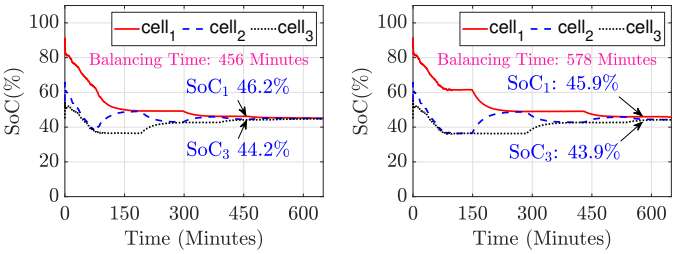

(a) Balancing speed of ideal SC

(b) Balancing speed of non-ideal SC

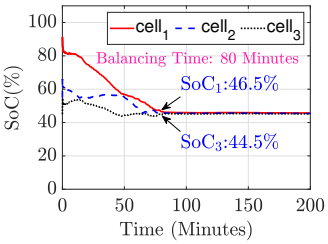

(c) Balancing speed of ideal BB

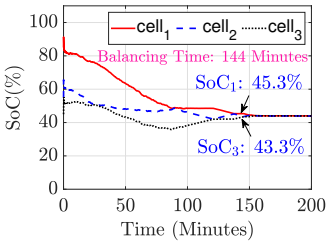

(d) Balancing speed of non-ideal BB

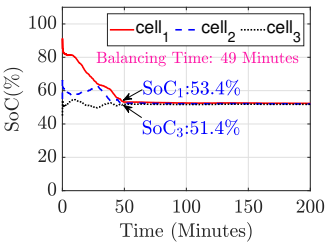

(e) Balancing speed of ideal FB

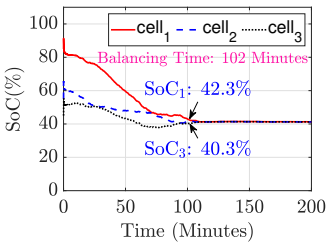

(f) Balancing speed of non-ideal FB

Fig. 6: Comparison of cell balancing speed of ACBNs

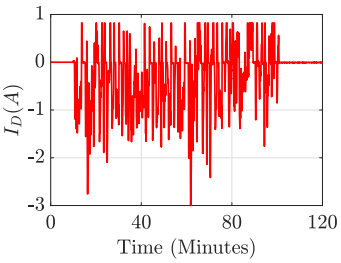

(a) UDDS current profile

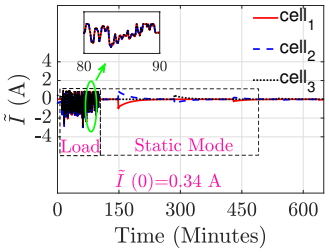

(b) Cell currents during cell balancing of non-ideal SC

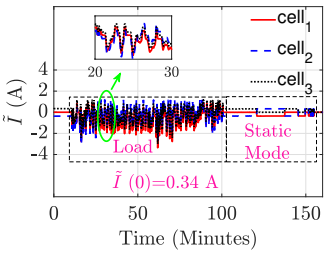

(c) Cell currents during cell balancing of non-ideal BB

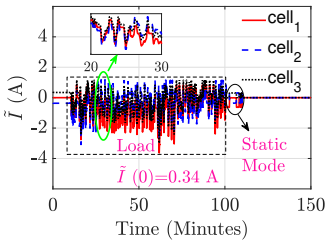

(d) Cell currents during cell balancing of FB

Fig. 7: Comparison of cell balancing currents of non-ideal ACBNs

where $\bar{P}_{in}$ and $\bar{P}_{losses}$ are average input power and average power losses due to conduction and switching, respectively.

The static and dynamic parameters of each ACBN are varied to perform a sensitivity analysis. The impact of static parameters is observed by varying the net resistances of the charging and discharging paths of energy storage elements at a constant t_d, and results are summarized in Table IV. It is observed that increasing the resistance from $R/5$ to $5R$ reduces the mean current, input power, total power losses, and efficiency of the SC network by 75.7%, 89.0%, 84.1%, and 0.57%, respectively. In contrast, the percentage changes for charging and discharging mean currents, input power, total power losses, and efficiency in BB network are -10.0%, -33.4%, -9.94%, +803.8%, and -3.6%, respectively. The FB network exhibits characteristics comparable to BB networks, and the corresponding percentage change in the charging and discharging mean currents, input power, total power losses, and efficiency are -10.0%, -35.6%, -10.5%, +816.1%, and -3.6%. Thus, it is pertinent to mention that the static parameters greatly influence the mean and RMS currents of the SC network as compared to BB and FB networks. In the SC network, both mean and RMS currents decrease when resistance increases, resulting in decreased input power and conduction losses. On the contrary, both BB and FB networks exhibit nearly identical behavior, with a little drop in current and input power and a significant rise in conduction losses. In all balancing networks, switching losses have an inverse relationship with resistances. The SC network, on the other hand, has the highest switching losses at similar resistance values. During the dead time, power losses in BB and FB networks diminish as resistances grow. However, there is no power loss in the SC network because no current flows during the dead time. The power losses caused by the body diode reverse recovery only affect BB and FB converters. Compared to BB and FB networks, total power losses in the SC network are considerably decreased with an increase in net resistance. Thereby, contrary to the SC network, the efficiency of inductive networks is more susceptible to an increase in net resistance. The effect of dynamic parameters on the performance of cell balancing networks is investigated by varying t_d and keeping the net resistance constant. Table V shows that increasing the dead time from $t_d/4$ to $2t_d$ results in a -22.8%, +6.6%, -20.4%, and +0.26% change in the mean current, input power, total power losses, and efficiency of the SC network, respectively. Whereas in a BB network, the percentage changes for the charging and discharging mean currents, input power, total power losses and efficiency are, in the order,-71.3%, -70.1%, -60.6%, -88.2%, and +1.2%. Similarly, the FB network's parameters' percentage deviations are -71.3%, -70.0%, -60.5%, -87.9%, and +1.3%, respectively. These results show that the mean and RMS currents of BB and FB networks are more affected by t_d than the SC network. Consequently, the input power delivered by the SC network has the least impact on t_d variation as compared to inductive networks. Since all balancing networks' mean and RMS currents are reduced by increasing t_d, which results in low power losses and increased efficiency.

Similarly, the impact of real parameters on the performance of the cell balancing architecture is determined by computing the deviation of η and $\tilde{I}$ from the ideal values. The percentage

TABLE IV: Effect of Static Parameters at constant $t_d = 2.0\mu s$

Parameters	Balancing type	$R/5$	$R/3$	R	$3R$	$5R$
$\tilde{I}_{out}(A)$	SC	0.70	0.70	0.59	0.27	0.17
	BB	0.60	0.60	0.59	0.57	0.54
	FB	0.60	0.6	0.59	0.56	0.54
$\tilde{I}_{in}(A)$	SC	0.70	0.70	0.59	0.27	0.17
	BB	0.59	0.58	0.55	0.46	0.39
	FB	0.59	0.58	0.54	0.45	0.38
$\tilde{P}_{in}(W)$	SC	11.43	8.85	4.9	2.03	1.25
	BB	5.03	5.02	4.95	4.73	4.53
	FB	5.03	5.02	4.94	4.71	4.50
$\tilde{P}_{cond}(mW)$	SC	84.6	84.4	70.5	32.8	20.4
	BB	9.2	15.1	42.8	110.1	161
	FB	9.8	16.2	45.7	117.2	170.6
$\tilde{P}_{sw}(mW)$	SC	56.4	33.8	10.8	3.4	2.0
	BB	0.832	0.46	0.44	0.37	0.31
	FB	0.47	0.46	0.43	0.36	0.3
$\tilde{P}_{t_d}(mW)$	SC	-	-	-	-	-
	BB	8.8	8.7	8.2	6.9	5.8
	FB	8.8	8.7	8.2	6.8	5.7
$\tilde{P}_{D_{RR}}(mW)$	SC	-	-	-	.-	-
	BB	0.048	0.048	0.048	0.048	0.048
	FB	0.2	0.2	0.2	0.2	0.2
$\tilde{P}_{total_{losses}}(mW)$	SC	141.0	118.2	81.3	36.2	22.4
	BB	18.5	24.3	51.4	117.4	167.2
	FB	19.3	25.5	54.5	124.6	176.8
$\eta(\%)$	SC	98.76	98.66	98.34	98.22	98.2
	BB	99.63	99.51	98.96	97.52	96.31
	FB	99.61	99.49	98.89	97.35	96.07

TABLE V: Effect of dynamic parameters at constant parasitic resistances

Parameters	Balancing type	$t_d/4$	$t_d/2$	t_d	$2t_d$
$\tilde{I}_{out}(A)$	SC	0.632	0.62	0.587	0.488
	BB	0.915	0.798	0.588	0.263
	FB	0.912	0.796	0.587	0.262
$\tilde{I}_{in}(A)$	SC	0.632	0.62	0.587	0.488
	BB	0.835	0.732	0.546	0.250
	FB	0.829	0.728	0.543	0.249
$\tilde{P}_{in}(W)$	SC	4.99	4.96	4.90	4.66
	BB	6.88	6.21	4.95	2.71
	FB	6.86	6.20	4.94	2.71
$\tilde{P}_{cond}(mW)$	SC	75.8	74.3	70.5	58.6
	BB	113.6	84.4	42.8	6.1
	FB	118.9	88.9	45.7	7.0
$\tilde{P}_{sw}(mW)$	SC	11.0	11.0	10.8	10.5
	BB	0.67	0.59	0.44	0.20
	FB	0.66	0.58	0.43	0.20
$\tilde{P}_{t_d}(mW)$	SC	-	-	-	-
	BB	3.1	5.5	8.2	7.5
	FB	3.1	5.5	8.2	7.5
$\tilde{P}_{D_{RR}}(mW)$	SC	-	-	-	-
	BB	0.048	0.048	0.048	0.048
	FB	0.20	0.20	0.20	0.20
$\tilde{P}_{total_{losses}}(mW)$	SC	86.8	85.2	81.3	69.1
	BB	117.4	90.5	51.4	13.8
	FB	122.9	95.1	54.5	14.9
$\eta(\%)$	SC	98.26	98.28	98.34	98.52
	BB	98.29	98.54	98.96	99.49
	FB	98.20	98.46	98.89	99.45

changes $\Delta\eta\%$ and $\Delta\tilde{I}\%$ are computed as

$$\Delta\eta\% = 100 \times \frac{\eta(Real) - \eta(Ideal)}{\eta(Ideal)}, \tag{33}$$

$$\Delta\tilde{I}\% = 100 \times \frac{\tilde{I}(Real) - \tilde{I}(Ideal)}{\tilde{I}(Ideal)}, \tag{34}$$

where $\eta(Real)$ and $\eta(Ideal)$ are the efficiency of real and ideal networks, respectively. While $\tilde{I}(Real)$ and $\tilde{I}(Ideal)$ are the mean balancing currents of real and ideal circuits, respectively.

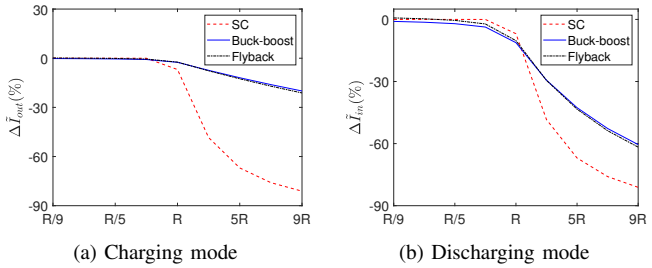

(a) Charging mode (b) Discharging mode

Fig. 8: Effect of static parameters on mean currents of ACBNs

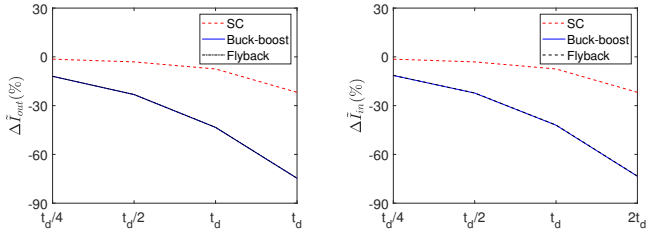

(a) Charging mode (b) Discharging mode

Fig. 9: Effect of dynamic parameters on mean currents of ACBNs

The effect of parasitic and on-state switch resistances on the mean currents of each balancing network during charging and discharging mode is shown in Fig. 8a and Fig. 8b, respectively. The deviation of mean currents from the ideal values in the SC network during charging and discharging modes is similar due to the equal net resistances of charging and discharging paths. The variation of mean current during discharging mode is evident in BB and FB networks due to the diode's forward voltage drop. However, this variation is less than that of the SC network. Thus, the reduction in average current is highest in the SC network, resulting in a large cell balancing time and reduction in input power. Moreover, it also impacts power losses and efficiency. It is worth noting in Fig. 10a that the decrease in average current reduces power losses and results in less deviation in the efficiency of the SC network as compared to the inductor-based techniques. The impact of dead time variation on the average current of cell balancing networks is shown in Fig. 9. It is observed that the average current decreases with the increase in t_d. The SC network has the least impact on t_d variation. The t_d reduces the effective duty cycle which leads to the reduction of balancing current, so it slows down the cell balancing speed but increases efficiency due to reduced power losses, as shown in Fig. 10b. The trade-off between the efficiency and cell balancing speed is highlighted by plotting a Pareto front, as shown in Fig. 11. It is observed that the average current has exponentially deviated at $\Delta\eta = 1.8\%$ for the SC network. While the deviation in average current with respect to $\Delta\eta$ is almost linear in BB and FB techniques. This indicates that the SC network is efficient but slower than inductive techniques.

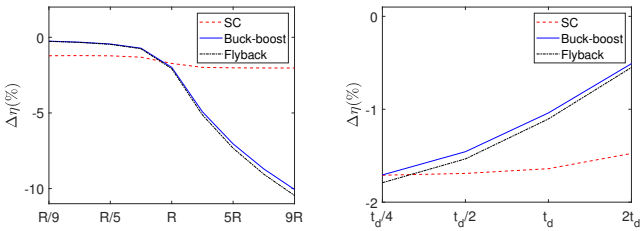

(a) Impact of static parameters (b) Impact of dynamic parameters

Fig. 10: Effect of static and dynamic parameters on efficiency of ACBNs.

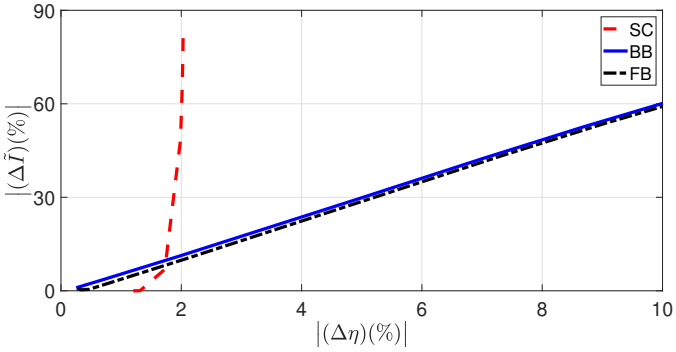

Fig. 11: Pareto front between cell balancing speed and efficiency of ACBNs.

VI. Conclusion

In this manuscript, the impact of static and dynamic parameters on the performance of ACBNs is highlighted. For this purpose, mean current models are formulated for SC, BB, and FB networks as a function of static and dynamic parameters. It is observed that the performance of each cell balancing network is sensitive to static and dynamic parameters. The percentage change in the cell balancing speed of SC, BB, and FB networks with static and dynamic parameters are 26.75%, 80%, and 108%, respectively. The sensitivity analysis shows that trade-off is exhibited in the balancing speed and efficiency of cell-balancing networks. It is observed that the static and dynamic parameters have the least impact on the efficiency of the SC network. While the impact on the efficiency of BB and FB networks are almost similar.

One of the possible extensions of the current work is the development of intelligent closed-loop system to achieve cell equalization in optimal manner. Moreover, incorporating advanced thermal management into the closed-loop active cell balancing systems offers a promising pathway to enhance battery efficiency, safety, and longevity.

References

[1] Q. Ouyang, Y. Zhang, N. Ghaeminezhad, J. Chen, Z. Wang, X. Hu, J. Li, Module-based active equalization for battery packs: A two-layer model predictive control strategy, IEEE Transactions on Transportation Electrification 8 (1) (2022) 149–159. doi:10.1109/TTE.2021.3095497.

[2] C. Duan, C. Wang, Z. Li, J. Chen, S. Wang, A. Snyder, C. Jiang, A solar power-assisted battery balancing system for electric vehicles, IEEE Transactions on Transportation Electrification 4 (2) (2018) 432–443.

[3] R. Paidi, S. K. Gudey, Active and passive cell balancing techniques for li-ion batteries used in evs, in: 2022 IEEE International Power and Renewable Energy Conference (IPRECON), 2022, pp. 1–6. doi:10.1109/IPRECON55716.2022.10059573.

[4] J. Carter, Z. Fan, J. Cao, Cell equalisation circuits: A review, Journal of Power Sources 448 (2020) 227489.

[5] Z. B. Omariba, L. Zhang, D. Sun, Review of battery cell balancing methodologies for optimizing battery pack performance in electric vehicles, IEEE Access 7 (2019) 129335–129352. doi:10.1109/access.2019.2940090.
URL http://dx.doi.org/10.1109/access.2019.2940090

[6] N. T. Milas, E. C. Tatakis, Fast battery cell voltage equaliser based on the bi-directional flyback converter, IEEE Transactions on Transportation Electrification (2022).

[7] S. B. Javed, A. A. Uppal, M. R. Azam, K. Shehzad, Q. Ahmed, Model-based quantitative analysis of a capacitive cell balancing technique using soc estimator, in: 2022 IEEE Conference on Control Technology and Applications (CCTA), 2022, pp. 670–675. doi:10.1109/CCTA49430.2022.9966110.

[8] A. A. Uppal, S. B. Javed, Q. Ahmed, Power losses aware nonlinear model predictive control design for active cell balancing, IEEE Control Systems Letters 7 (2023) 3705–3710. doi:10.1109/lcsys.2023.3342550.
URL http://dx.doi.org/10.1109/lcsys.2023.3342550

[9] H. S, Overview of cell balancing methods for li-ion battery technology, Energy Storage 3 (2) (Sep. 2020). doi:10.1002/est2.203.
URL http://dx.doi.org/10.1002/est2.203

[10] P. Jadhav, M. Murali, A. Bagade, A. Mandhana, Comparative analysis of cell balancing techniques and development of active cell balancing model using inductor, in: 2023 5th International Conference on Energy, Power and Environment: Towards Flexible Green Energy Technologies (ICEPE), 2023, pp. 1–6. doi:10.1109/ICEPE57949.2023.10201526.

[11] F. Qu, Q. Luo, H. Liang, D. Mou, P. Sun, X. Du, Systematic overview of active battery equalization structures: Mathematical modeling and performance evaluation, IEEE Transactions on Energy Conversion 37 (3) (2022) 1685–1703.

[12] G. Sugumaran, N. Amutha Prabha, et al., A comprehensive review of various topologies and control techniques for dc-dc converter-based lithium-ion battery charge equalization, International Transactions on Electrical Energy Systems 2023 (2023).

[13] Y. Hua, S. Zhou, H. Cui, X. Liu, C. Zhang, X. Xu, H. Ling, S. Yang, A comprehensive review on inconsistency and equalization technology of lithium-ion battery for electric vehicles, International Journal of Energy Research 44 (14) (2020) 11059–11087.

[14] Y. Shang, B. Xia, C. Zhang, N. Cui, J. Yang, C. C. Mi, An automatic equalizer based on forward–flyback converter for series-connected battery strings, IEEE Transactions on Industrial Electronics 64 (7) (2017) 5380–5391.

[15] J. Gallardo-Lozano, E. Romero-Cadaval, M. I. Milanes-Montero, M. A. Guerrero-Martinez, Battery equalization active methods, Journal of Power Sources 246 (2014) 934–949.

[16] N. Ghaeminezhad, Q. Ouyang, X. Hu, G. Xu, Z. Wang, Active cell equalization topologies analysis for battery packs: A systematic review, IEEE Transactions on Power Electronics 36 (8) (2021) 9119–9135.

[17] M. Preindl, C. Danielson, F. Borrelli, Performance evaluation of battery balancing hardware, in: 2013 European Control Conference (ECC), IEEE, 2013, pp. 4065–4070.

[18] F. Baronti, R. Roncella, R. Saletti, Performance comparison of active balancing techniques for lithium-ion batteries, Journal of Power Sources 267 (2014) 603–609.

[19] M. Caspar, T. Eiler, S. Hohmann, Comparison of active battery balancing systems, in: 2014 IEEE Vehicle Power and Propulsion Conference (VPPC), IEEE, 2014, pp. 1–8.

[20] M. Caspar, T. Eiler, S. Hohmann, Systematic comparison of active balancing: A model-based quantitative analysis, IEEE Transactions on Vehicular Technology 67 (2) (2016) 920–934.

[21] D. Thiruvonasundari, K. Deepa, Evaluation and comparative study of cell balancing methods for lithium-ion batteries used in electric vehicles., International Journal of Renewable Energy Development 10 (3) (2021).

[22] M. R. Azam, A. Ahmad, A. A. Uppal, Q. Ahmed, Nonlinear model predictive control design for active cell balancing and thermal management, in: 2024 IEEE Conference on Control Technology and Applications (CCTA), IEEE, 2024.

[23] M. Al-Gabalawy, N. S. Hosny, J. A. Dawson, A. I. Omar, State of charge estimation of a li-ion battery based on extended kalman filtering and sensor bias, International Journal of Energy Research 45 (5) (2021) 6708–6726.

[24] P. Kollmeyer, C. Vidal, M. Naguib, M. Skells, Lg 18650hg2 li-ion battery data and example deep neural network xev soc estimator script, Mendeley Data 3 (2020).